



Capability of Searching for Kilonova Associated with a Short Gamma-Ray Burst by SVOM

J. Wang^{1,2}, L. P. Xin¹, Y. L. Qiu¹, L. Lan¹, W. J. Xie¹, Z. P. Jin³, and J. Y. Wei¹

¹ Key Laboratory of Space Astronomy and Technology, National Astronomical Observatories, Chinese Academy of Sciences, Beijing 100101, China; wj@nao.cas.cn

² Guangxi Key Laboratory for Relativistic Astrophysics, School of Physical Science and Technology, Nanning 530004, China

³ Key Laboratory of Dark Matter and Space Astronomy, Purple Mountain Observatory, Chinese Academy of Sciences, Nanjing 210023, China

Received 2024 July 20; revised 2024 August 28; accepted 2024 September 23; published 2024 October 30

Abstract

In spite of the importance of studying the cosmic generation of heavy elements through the *r*-process, the detection of a kilonova resulting from the merger of a neutron star binary is still a challenging task. In this paper, we show that the Visible Telescope (VT) onboard the ongoing SVOM space mission is powerful for identifying kilonova candidates associated with short gamma-ray bursts up to a distance of 600 Mpc. A significant color variation, turning blue and then turning red, is revealed by calculating the light curves in both red and blue channels of VT by a linear combination of an afterglow and an associated kilonova. The maximum color variation is as high as $\sim 0.5\text{--}1$ mag, which is far larger than the small photometry error of ~ 0.2 mag of VT for a point source with a brightness of 23 mag. Up to a distance of 600 Mpc, $\sim 1\text{--}2$ kilonova candidates per year are predicted to be identified by VT.

Key words: instrumentation: photometers – telescopes – stars: neutron – (stars:) gamma-ray burst: general

1. Introduction

The merger of a neutron star binary in the Hubble timescale is predicted to manifest itself as gravitational wave (GW) radiation (e.g., Abbott et al. 2020), a short-duration gamma-ray burst (SGRB, $T_{90} < 2$ s, e.g., Kouveliotou et al. 1993), and an associated kilonova (e.g., Eichler et al. 1989; Li & Paczyński 1998; Freiburghaus et al. 1999; Rosswog et al. 1999; Perego et al. 2014; Just et al. 2015). The kilonova is powered by the radioactive decay of isotopes of the heavy elements that are assembled by the so-called rapid neutron capture (*r*-process) nucleosynthesis in the matter expelled by the merger (e.g., Burbidge et al. 1957; Metzger et al. 2010; Korobkin et al. 2012; Barnes & Kasen 2013; Kasen et al. 2013, 2017; Barnes et al. 2016; Metzger 2019; Chen et al. 2024).

Although SGRBs have been frequently detected by past and ongoing gamma-ray burst (GRB) missions (see review in Berger 2014), the detection of the associated kilonova is still a hard task at the current stage (e.g., Troja 2023). In fact, only two have been confirmed by spectroscopy in literature. The first case, AT 2017gfo associated with a weak SGRB GRB 170817A, was found by the Swope Supernova Survey during a campaign of searching for the electromagnetic counterpart of GW170817 discovered by the LIGO-Virgo experiments (e.g., Abbott et al. 2017a, 2017b; Andreoni et al. 2017; Arcavi et al. 2017; Covino et al. 2017; Cowperthwaite et al. 2017; Drout et al. 2017; Evans et al. 2017; Goldstein et al. 2017; Kilpatrick et al. 2017; Smartt et al. 2017; Tanaka et al. 2017). The

identification of the kilonova was confirmed by comparing its spectroscopic sequence obtained by large telescopes with the spectral models (e.g., Pian et al. 2017; Shappee et al. 2017). The second one is GRB 230307A, a long-duration GRB at $z = 0.065$, in which Levan et al. (2024) recently identified an emission-line of tellurium (atomic mass $A = 130$) and a very red spectral-energy distribution from the mid-infrared spectroscopy and imaging taken by the James Webb Space Telescope dozens of days after the trigger.

In addition to the two spectroscopically confirmed cases, by modeling the multi-wavelength light curves, a batch of kilonova candidates has been identified due to an excess of near-infrared (NIR) emission a couple of days after the GRBs' trigger (e.g., Berger et al. 2013; Fan et al. 2013; Tanvir et al. 2013; Jin et al. 2015, 2016, 2018, 2020, 2021; Yang et al. 2015; Troja et al. 2018, 2019; Lamb et al. 2019; Rastinejad et al. 2022; Zhu et al. 2023; Troja et al. 2022; Yang et al. 2024).

In this paper, we demonstrate that the Visible Telescope (VT) onboard the Space Variable Objects Monitor (SVOM) satellite enables us to easily identify kilonova candidates up to a distance of ~ 600 Mpc according to their strong NIR excess. The main reason for this fact is that the red channel of VT has quite deep sensitivity up to a wavelength of $1\ \mu\text{m}$ because of the lack of strong NIR atmospheric emission in space. The paper is organized as follows. Section 2 briefly describes the payloads of the SVOM mission, especially the capability of VT. The calculations of the optical light curves observed by VT

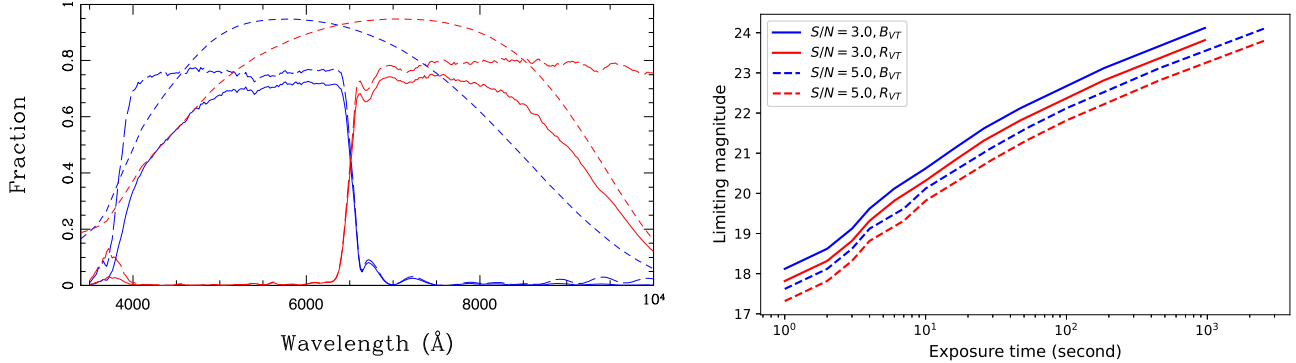


Figure 1. Left panel: The total throughput curves (the solid lines), transmittance of the filters (the long-dashed lines) and QE of the CCDs (the short-dashed lines) of VT as a function of wavelength. The blue and red channels are signified by blue and red colors, respectively. Right panel: The predicted limiting magnitudes in both VT channels plotted against exposure time at two significance levels, i.e., 3σ and 5σ .

are presented in Section 3. Section 4 gives the results and implication. Conclusions are stated in Section 5.

2. Instruments Onboard SVOM

SVOM, launched on 2024 June 22, is a Chinese-French space mission dedicated to the detection and study of GRBs. We refer the readers to Atteia et al. (2022) and the white paper given by Wei et al. (2016) for the details.

There are four onboard instruments. The wide-field soft γ -ray imager ECLAIRs and Gamma-Ray Monitor (GRM) are designed to observe GRB prompt emission in 4–150 keV and 15–5000 keV energy bands, respectively. With a field-of-view (FoV) of 2 sr and a sensitivity of 7.2×10^{-10} erg s $^{-1}$ cm $^{-2}$ (5σ detection level in an exposure of 1000 s), a total of 60–70 GRBs per year can be triggered by ECLAIRs (Godet et al. 2014; Cordier et al. 2015). In addition, with a detection area of 200 cm 2 for each Gamma-Ray Detector (GRD) module, ~90 GRBs are expected to be detected per year by GRM.

The narrow-field Microchannel X-ray Telescope (MXT, Gotz et al. 2014) and VT are responsible for follow-up observations of the afterglows in X-ray and optical wavelengths, respectively. VT is a Ritchey-Chrétien telescope with a 43 cm diameter and an f -ratio of 9. It has an FoV of about 26×26 arcmin 2 , covering ECLAIR's error box in most cases. The limiting magnitude is down to $m_V = 22.5$ mag for a 300 s exposure. With a dichroic beam splitter, VT works in two channels, one in blue and the other in red, simultaneously. The blue channel has a wavelength range from 0.4 to 0.65 μ m, and the red one from 0.65 to 1.0 μ m. Each channel is equipped with a 2k \times 4k E2V frame transfer CCD, in which a back-illuminated thick CCD is used for the red channel to enhance the quantum efficiency (QE).

The left panel in Figure 1 shows the total throughput curves of the two channels, along with the corresponding transmittance of the filters and the QE of the two CCDs. A more detailed description of the calibration and determination of the

throughput curves can be found in Y. L. Qiu et al. (2024, in preparation). With the throughput curves, the limiting magnitudes in the two channels are calculated by the dedicated Exposure Calculator of VT⁴ according to the simplified “CCD” equation (Mortara & Fowler 1981; Gullixson 1992; Merline & Howell 1995 and see NOAO/KPNO CCD instrument manuals)

$$\frac{S}{N} \simeq \frac{\eta N_* t}{\sqrt{\eta N_* t + n_{\text{pix}}(\eta N_b t + N_d t + RN^2)}}, \quad (1)$$

where N_* , N_b and N_d are the photon rate from the source, the photon rate per pixel from sky background, and dark current per pixel, respectively. t is the exposure time and RN the readout noise of each pixel. n_{pix} and η are the number of pixels occupied by a single star and the system total throughput, respectively. The calculated limiting magnitudes (see Section 3.3 for the definition of magnitude of SVOM/VT) in both channels are plotted in the right panel of Figure 1 as a function of exposure time for a powerlaw $f_\nu \propto \nu^{-1.3}$ (typical of a GRB, see below) at two significance levels of 3σ and 5σ . Basically, for an exposure of 300 s, the limiting magnitudes are 23.4 and 23.1 for the blue and red channels, respectively, at a significance level of 3σ . The corresponding values degrade to 22.9 and 22.6 at a significance level of 5σ .

3. Calculation of Theoretical Light Curves

To examine the capability of identifying kilonova candidates, we calculate a set of light curves recorded in both VT channels by a linear combination of an SGRB's afterglow and an associated kilonova.

⁴ The calculator can be visited at the website of SVOM Science User Support System through the link <https://svom-gwacn.cn/gp/tools/CalcExptimeVT.action>.

3.1. Afterglow from SGRB

The evolution of the luminosity of an afterglow is calculated by adopting the simple and widely used powerlaw: $L_\nu^{\text{grb}} \propto \nu^{-\alpha} t^{-\beta}$. The values of α and β are fixed to be 1.3 and 1.2, respectively, for a late afterglow (i.e., at about 1 day after a trigger and ignoring the possible jet break effect) throughout the paper. The coefficient of the powerlaw is determined from a sample of the normalized light curves of SGRBs (e.g., Nicuessa Guelbenzu et al. 2012). Specifically, the brightness in the R_c -band at 1 day is adopted to be from 29 to 25 mag in the $z = 1$ reference frame.

3.2. Emission from Kilonova

The spectral model grid developed by Kasen et al. (2017)⁵ is adopted by us to calculate the specific luminosity L_ν^{kn} of a given kilonova at a given time. In the model, the mergers of two neutron stars are simulated in general relativity, in which the material is ejected by two distinct ways. One with a high velocity of 0.2–0.3c results from the dynamical expelling of the matter from the surface of the approaching stars due to the tidal force, along with the squeezing of the matter at the interface. The other low-velocity (0.05–0.1c) ejection is caused by the wind from the accretion disk formed around the central remnant after the merger. The ejecta is assumed to be spherically symmetric with a density profile of $\propto v^{-1}$ and $\propto v^{-10}$ in the inner and outer layers, respectively. The emission resulting from the decay of radioactive r -process isotopes is calculated by solving the time-dependent radiative transfer equation under local thermodynamic equilibrium, in which millions of bound-bound transitions are considered to obtain the opacities, including all lanthanides.

The model grid provides spectra from ultraviolet to infrared every 0.1 days after a merger. In addition to the fixed exponents of the inner and outer density profile, the parameters of the model grid are: the ejecta mass $0.001 \leq m/M_\odot \leq 0.1$, the kinetic velocity of the ejecta $0.03 \leq v_k/c \leq 0.3$ and the mass fraction of lanthanides $10^{-9} \leq X_{\text{lan}} \leq 10^{-1}$.

3.3. Predicted Light Curves Recorded by VT

With the time resolved spectra of both afterglow and kilonova described above, the light curves recorded in the two VT channels (denoted by B_{VT} and R_{VT} for the blue and red channels, respectively) are calculated according to the definition of the AB magnitude (Fukugita et al. 1996)

$$m_{\text{AB}} = -2.5 \log \frac{\int f_\nu S_\nu d\ln\nu}{\int S_\nu d\ln\nu} - 48.6, \quad (2)$$

where S_ν is the total throughput at frequency ν as given in Figure 1. f_ν is the specific flux density of an object in the unit of

⁵ https://github.com/dnkasen/Kasen_Kilonova_Models_2017

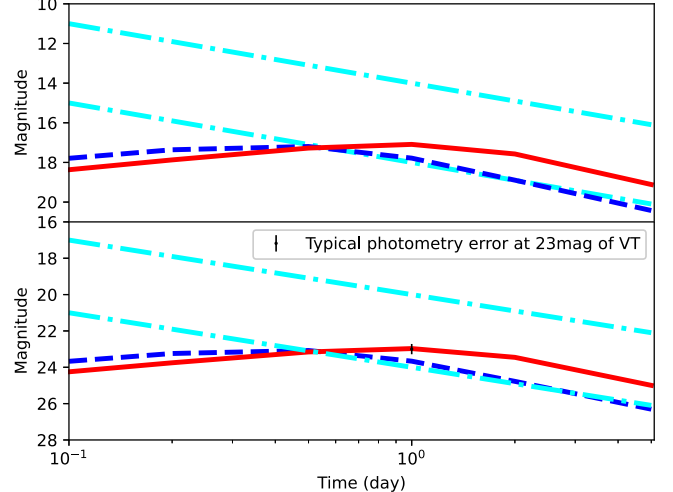


Figure 2. Calculated light curves of an afterglow and a kilonova for a distance of 40 Mpc (upper panel) and 600 Mpc (lower panel). In each panel, the two cyan dot-dashed lines correspond to the light curves of an afterglow with $R_c = 25$ and 29 mag, the brightness in the R_c -band at 1 day in the $z = 1$ reference frame. The red-solid and blue-dashed lines are the kilonova light curves recorded in VT red and blue channels, respectively. See the text for the details of calculations. The vertical black line in the lower panel marks the typical magnitude error of ~ 0.2 mag measured by VT for a source with a brightness of 23 mag.

$\text{erg s}^{-1} \text{cm}^{-2} \text{Hz}^{-1}$, and is calculated from the predicted luminosity L_ν as $f_\nu = L_\nu / 4\pi d^2$, where d is the distance.

4. Results

Figure 2 compares the predicted light curves between an afterglow and a kilonova both at a distance of 40 Mpc (the upper panel) and 600 Mpc (the lower panel). In each panel, the boundaries of the afterglow are inferred for the two extreme cases, i.e., a strong afterglow with $m_{R_c} = 25$ mag and a weak afterglow with $m_{R_c} = 29$ mag, where m_{R_c} is the brightness in the R_c -band at 1 day in the $z = 1$ reference frame. The kilonova light curves are obtained from the model spectra with $m = 0.05 M_\odot$, $v_k = 0.3c$ and $X_{\text{lan}} = 10^{-4}$.

Three facts can be learned from the figure. At first, the two VT channels reproduce the well known infrared excess of a kilonova at the late epoch of ~ 1 day, which will be addressed below in more detail. Second, in the red channel, the light curve at ~ 1 day after a trigger can be dominated by a kilonova if the associated afterglow is quite weak (or off-axis). Finally, with the limiting magnitude of ~ 22.5 mag, a kilonova candidate can be identified in the VT red channel at a distance as far as ~ 600 Mpc.

Figure 3 shows the predicted temporal evolution of $B_{\text{VT}} - R_{\text{VT}}$ color obtained by VT for the whole kilonova spectral model grid given in Kasen et al. (2017). The fiducial model is again adopted to be the one with $m = 0.05 M_\odot$, $v_k = 0.3c$ and $X_{\text{lan}} = 10^{-4}$. In

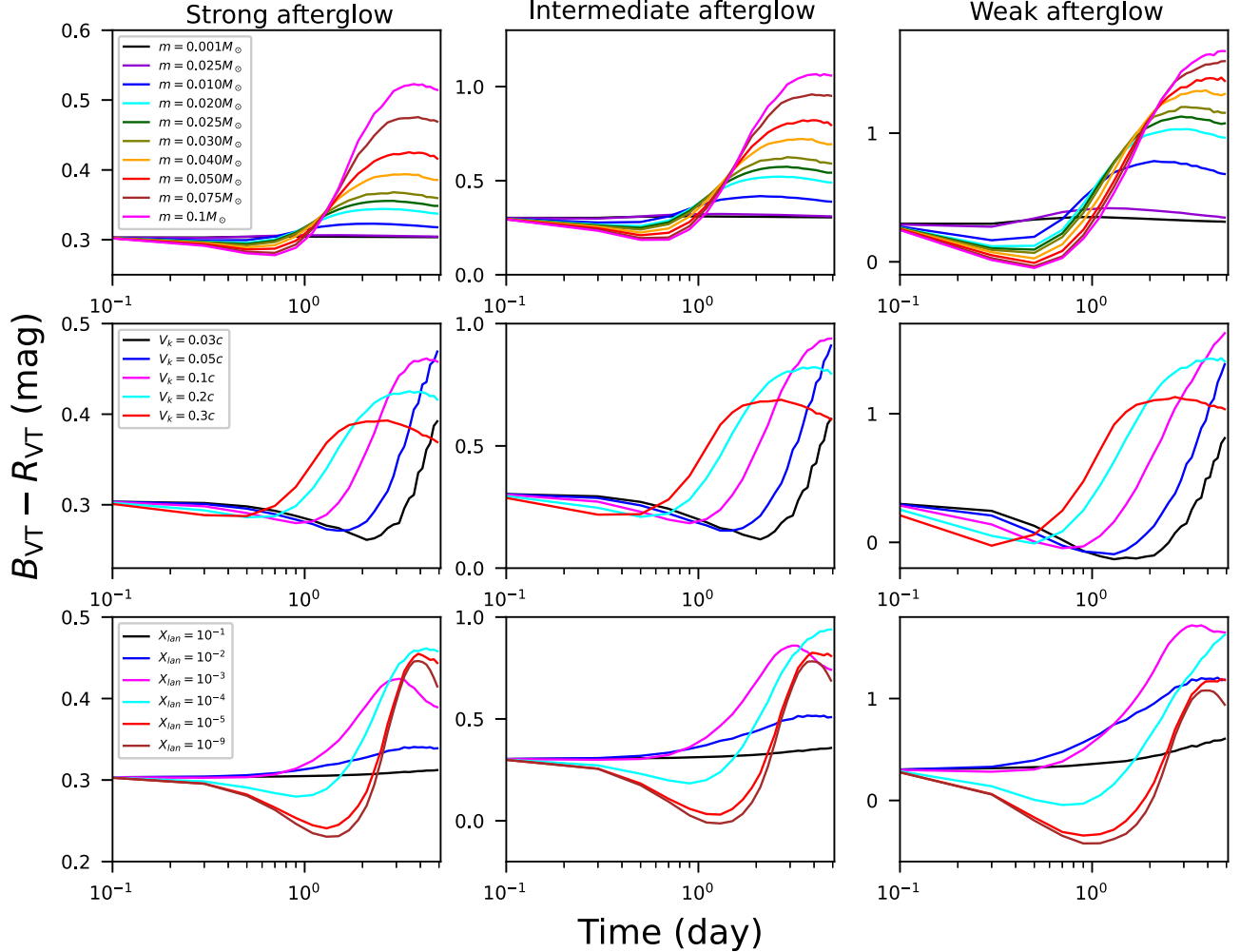


Figure 3. Evolution of the VT $B_{\text{VT}} - R_{\text{VT}}$ color assessed by a linear combination of an SGRB’s afterglow and a kilonova. The three columns correspond to different afterglow levels. The dependences on the ejecta mass (m), kinetic velocity of the ejecta (v_k) and mass fraction of lanthanides X_{lan} are displayed in the top, middle and bottom rows, respectively. See the main text for the details of the calculations.

addition to the strong and weak afterglow cases, the cases with an intermediate afterglow level with $m_{R_c} = 27$ mag are shown in the middle column. One can see from the figure a significant color variation in almost all the cases, in which the light curves become blue at early epoch, and transform to red at late epoch. The weaker the associated afterglow, the larger the value of color difference $\Delta(B_{\text{VT}} - R_{\text{VT}})$ will be. The maximum $\Delta(B_{\text{VT}} - R_{\text{VT}})$ is as high as $\sim 0.5\text{--}1$ mag. It is noted that $\Delta(B_{\text{VT}} - R_{\text{VT}})$ is in fact independent of the spectral shape of the associated afterglow as long as its spectral index stays constant. This revealed trend is consistent with the theoretical evolution of a kilonova, where the kilonova spectrum is dominated by the “blue” (light r -process) component at the beginning, and then by the “red” (heavy r -process) component after a couple of days.

We argue that there is an agreement between the spectral model and the dependence of the calculated color evolution on

kilonova parameters. At first, the top row in Figure 3 shows that a brighter kilonova that results in a redder spectrum is produced by a larger ejecta mass, which is consistent with the scaling law for the characteristic luminosity $L \propto m^{0.35}v^{0.65}\kappa^{-0.65}$, i.e., Equation (3) in Kasen et al. (2017), where κ is the opacity being sensitive to X_{lan} : the larger the X_{lan} , the larger the κ will be. Second, Equation (2) in Kasen et al. (2017) leads to a duration of kilonova $t \propto m^{1/2}v^{-1/2}\kappa^{1/2}$. This scaling law implies a shorter-lasting kilonova for a higher velocity, which can be learned from the middle row in the figure. Finally, the bottom row in the figure shows the dependence on X_{lan} . For the cases with a large $X_{\text{lan}} > 10^{-2}$, the corresponding large opacity causes a kilonova emission primarily appearing in infrared (i.e., the heavy r -process component), which results in a reduced effect on the optical color. On the contrary, a large variation of optical color can be revealed in the cases with small $X_{\text{lan}} < 10^{-4}$, in which the

kilonova emission in the optical bands is dominated by the light r -process component that decays and cools with time.

Based on our calculations, we conclude that VT is powerful for identifying a kilonova associated with an SGRB through the measured color variation of the afterglow. In fact, VT has typical photometry errors of ~ 0.01 and ~ 0.2 mag for a point source with brightness of 16 and 23 mag, respectively, which enable us to identify a kilonova candidate at a distance of up to 600 Mpc by VT. At this distance, in the case with a strong associated afterglow, the $B_{\text{VT}} - R_{\text{VT}}$ color is predicted to change by ~ 0.4 mag for the fiducial kilonova model with $m = 0.05 M_{\odot}$, $v_k = 0.3c$ and $X_{\text{lan}} = 10^{-4}$ (i.e., the red lines in Figure 3). This predicted color change is slightly larger than or comparable to the error of the measured color of $\sqrt{2} \times 0.2 \approx 0.3$ mag.

5. Conclusion and Implications

The light curves in both red and blue channels of VT onboard the SVOM satellite are predicted by a linear combination of an afterglow of an SGRB and an associated kilonova. The predicted light curves show a significant color variation with the maximum value as high as ~ 0.5 –1 mag. With the detection limit and accuracy, VT is therefore powerful for identifying kilonova candidates up to a distance of 600 Mpc.

We estimate the detection rate of kilonovae by VT as follows. Based on the recent BATSE GRB catalog,⁶ there are 500 SGRBs with $T_{90} < 2$ s among the 2041 events, which yield an SGRB fraction of $\sim 1/4$ in the BATSE sample. Since the GRM onboard SVOM has a comparable energy range with BASTE, ~ 20 SGRBs in total are predicted to be detected per year by GRM. Among the 20 SGRBs, there are ~ 1 –2 SGRBs with a luminosity distance up to 600 Mpc by assuming the SGRBs detected by GRM follow the redshift distribution of SGRBs given in Berger (2014), which lead to a kilonova detection rate of ~ 1 –2 yr^{−1} by VT onboard the SVOM.

Acknowledgments

The authors would like to thank the anonymous referee for their careful review and helpful comments. This study is supported by the Strategic Pioneer Program on Space Science, Chinese Academy of Sciences, grant XDB0550401. J.W. is supported by the National Natural Science Foundation of China (NSFC, grant No. 12173009), by the Natural Science Foundation of Guangxi (2020GXNSFDA238018) and by the Bagui Young Scholars Program. L.L. is supported by the National Postdoctoral Program for Innovative Talents (grant No. GZB20230765).

⁶ <https://gamma-ray.nsstc.nasa.gov/batse/grb/catalog/current/>

References

- Abbott, B. P., Abbott, R., Abbott, T. D., et al. 2017a, *ApJL*, **850**, L40
- Abbott, B. P., Abbott, R., Abbott, T. D., et al. 2017b, *ApJL*, **851**, L16
- Abbott, B. P., Abbott, R., Abbott, T. D., et al. 2020, *LRR*, **23**, 3
- Andreoni, I., Ackley, K., Cooke, J., et al. 2017, *PASP*, **34**, e069
- Arcavi, I., Hosseinzadeh, G., Howell, D. A., et al. 2017, *Natur*, **551**, 64
- Atteia, J.-L., Cordier, B., & Wei, J. 2022, *IMPD*, **31**, 2230008
- Barnes, J., & Kasen, D. 2013, *ApJ*, **775**, 18
- Barnes, J., Kasen, D., Wu, M.-R., et al. 2016, *ApJ*, **829**, 110
- Berger, E. 2014, *ARA&A*, **52**, 43
- Berger, E., Fong, W., & Chornock, R. 2013, *ApJL*, **774**, L23
- Burbidge, E.M., Burbidge, G.R., Fowler, W.A., & Hoyle, F. 1957, *RvMP*, **29**, 547
- Chen, M.-H., Li, L.-X., Chen, Q.-H., et al. 2024, *MNRAS*, **529**, 1154
- Cordier, B., Wei, J., Atteia, J. L., et al. 2015, arXiv:1512.03323
- Covino, S., Wiersema, K., Fan, Y. Z., et al. 2017, *NatAs*, **1**, 791
- Cowperthwaite, P. S., Berger, E., Villar, V. A., et al. 2017, *ApJL*, **848**, L17
- Drouet, M. R., Piro, A. L., Shappee, B. J., et al. 2017, *Sci.*, **358**, 1570
- Eichler, D., Livio, M., Piran, T., et al. 1989, *Natur*, **340**, 126
- Evans, P. A., Cenko, S. B., Kennea, J. A., et al. 2017, *Sci.*, **358**, 1565
- Fan, Y.-Z., Wu, X.-F., & Wei, D.-M. 2013, *PhRvD*, **88**, 067304
- Freiburg Haus, C., Rosswog, S., & Thielemann, F.-K. 1999, *ApJL*, **525**, L121
- Fukugita, M., Ichikawa, T., Gunn, J. E., et al. 1996, *AJ*, **111**, 1748
- Godet, O., Nasser, G., Atteia, J., et al. 2014, Proc. SPIE, 9144, 914424
- Goldstein, A., Veres, P., Burns, E., et al. 2017, *ApJL*, **848**, L14
- Gotz, D., Adamo, C., Basa, S., et al. 2014, in Proc. of Swift: 10 Years of Discovery (SWIFT 10), ed. P. Caraveo, P. D'Avanzo, N. Gehrels et al. (Trieste: SISSA)
- Gullixson, C. A. 1992, in ASPC: Astronomical CCD observing and reduction techniques, 23, ed. S. B. Howell (San Francisco, CA: ASP), 139
- Jin, Z.P., Covino, S., Liao, N.H., et al. 2020, *NatAs*, **4**, 77
- Jin, Z.-P., Hotokezaka, K., Li, X., et al. 2016, *NatCo*, **7**, 12898
- Jin, Z.-P., Li, X., Cano, Z., et al. 2015, *ApJ*, **811**, L22
- Jin, Z.-P., Li, X., Wang, H., et al. 2018, *ApJ*, **857**, 128
- Jin, Z. P., Zhou, H., Covino, S., et al. 2021, arXiv:2109.07694
- Just, O., Obergaulinger, M., & Janka, H.-T. 2015, *MNRAS*, **453**, 3386
- Kasen, D., Badnell, N. R., & Barnes, J. 2013, *ApJ*, **774**, 25
- Kasen, D., Metzger, B., Barnes, J., et al. 2017, *Natur*, **551**, 80
- Kilpatrick, C. D., Foley, R. J., Kasen, D., et al. 2017, *Sci.*, **358**, 1583
- Korobkin, O., Rosswog, S., Arcones, A., et al. 2012, *MNRAS*, **426**, 1940
- Kouveliotou, C., Meegan, C. A., Fishman, G. J., et al. 1993, *ApJL*, **413**, L101
- Lamb, G. P., Tanvir, N. R., Levan, A. J., et al. 2019, *ApJ*, **883**, 48
- Levan, A. J., Gompertz, B. P., Salafia, O. S., et al. 2024, *Natur*, **626**, 737
- Li, L.-X., & Paczyński, B. 1998, *ApJL*, **507**, L59
- Metzger, B. D. 2019, *LRR*, **23**, 1
- Metzger, B. D., Martínez-Pinedo, G., Darbha, S., et al. 2010, *MNRAS*, **406**, 2650
- Nicuesa Guelbenzu, A., Klose, S., Greiner, J., et al. 2012, *A&A*, **548**, A101
- Merline, W.J., & Howell, S.B. 1995, *ExA*, **6**, 163
- Mortara, L., & Fowler, A. 1981, in SPIE Conference Proceedings, 290, 28
- Perego, A., Rosswog, S., Cabezón, R. M., et al. 2014, *MNRAS*, **443**, 3134
- Pian, E., D'Avanzo, P., Benetti, S., et al. 2017, *Natur*, **551**, 67
- Rastinejad, J. C., Gompertz, B. P., Levan, A. J., et al. 2022, *Natur*, **612**, 223
- Rosswog, S., Liebendorfer, M., Thielemann, F.-K., et al. 1999, *A&A*, **341**, 499
- Shappee, B. J., Simon, J. D., Drouet, M. R., et al. 2017, *Sci.*, **358**, 1574
- Smartt, S. J., Chen, T.-W., Jerkstrand, A., et al. 2017, *Natur*, **551**, 75
- Tanaka, M., Utsumi, Y., Mazzali, P. A., et al. 2017, *PASJ*, **69**, 102
- Tanvir, N. R., Levan, A. J., Fruchter, A. S., et al. 2013, *Natur*, **500**, 547
- Troja, E. 2023, *Univ*, **9**, 245
- Troja, E., Fryer, C. L., O'Connor, B., et al. 2022, *Natur*, **612**, 228
- Troja, E., Ryan, G., Piro, L., et al. 2018, *NatCo*, **9**, 4089
- Troja, E., Castro-Tirado, A. J., Becerra Gonzlez, J., et al. 2019, *MNRAS*, **489**, 2104
- Wei, J. Y., Cordier, B., Antier, S., et al. 2016, arXiv:astro-ph/1610.0689
- Yang, B., Jin, Z. -P, Li, X., et al. 2015, *NatCo*, **6**, 7323
- Yang, Y. -H., Troja, E., O'Connor, B., et al. 2024, *Natur*, **626**, 742
- Zhu, Y.-M., Zhou, H., Wang, Y., et al. 2023, *MNRAS*, **521**, 269